Supplementary Information

Real-time single-molecule co-immunoprecipitation analyses reveal cancer-specific Ras signaling dynamics

Hong-Won Lee, Taeyoon Kyung, Janghyun Yoo, Tackhoon Kim, Chaeuk Chung, Ji Young Ryu, Hanki Lee, Kihyun Park, Sagnkyu Lee, Walton D. Jones, Dae-Sik Lim, Changbong Hyeon, Won Do Heo and Tae-Young Yoon
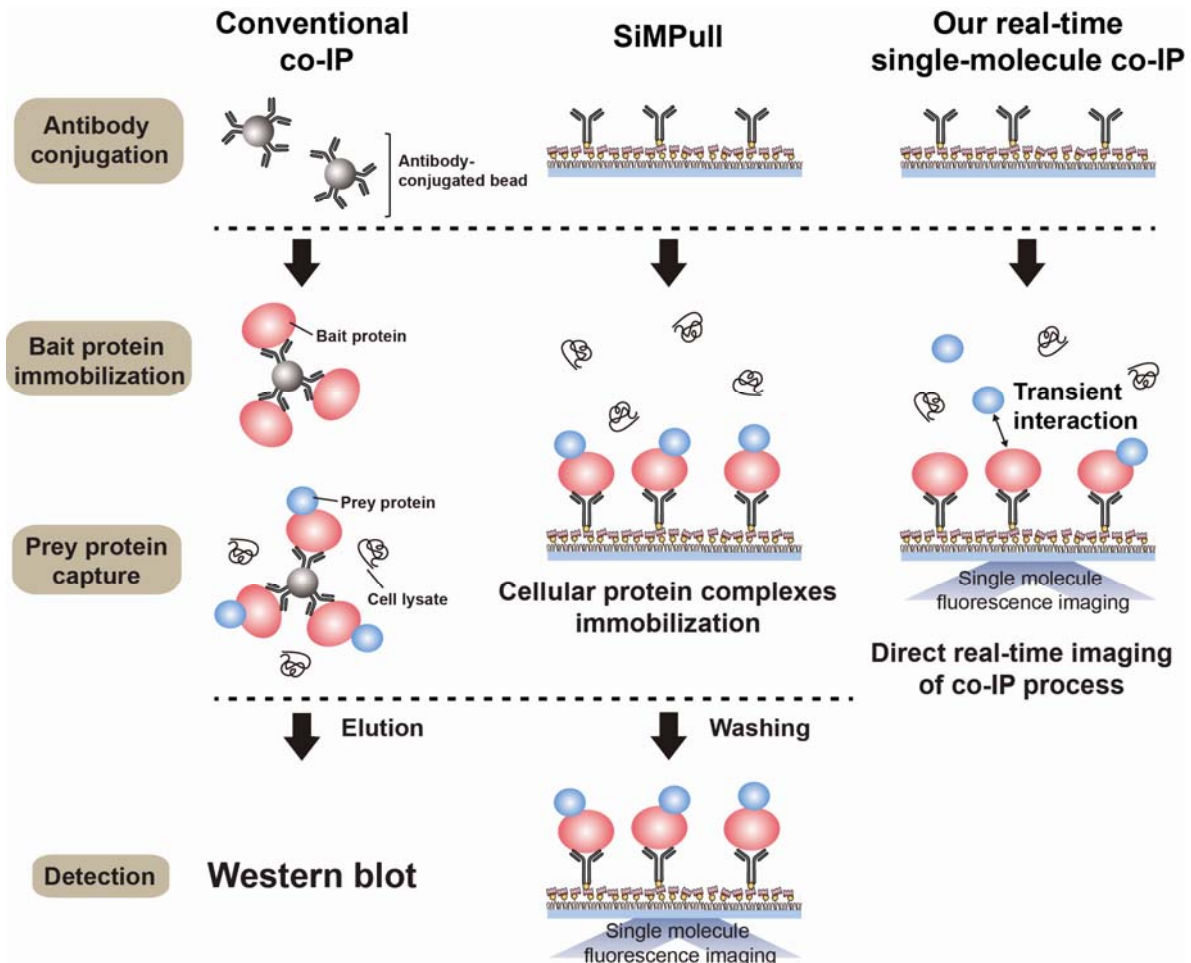
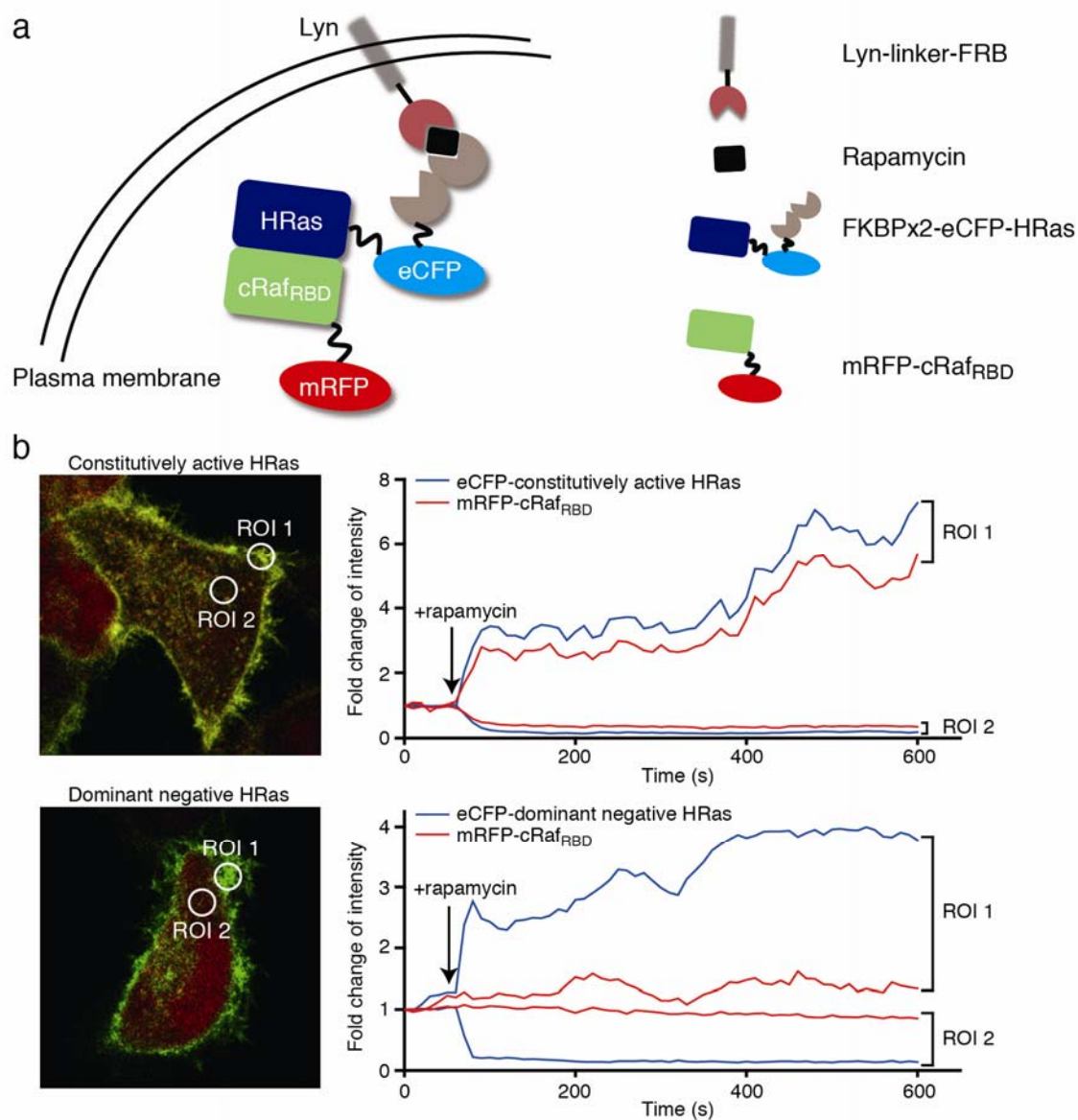Supplementary Figures S1 to S16

Supplementary Table S1

Supplementary Methods
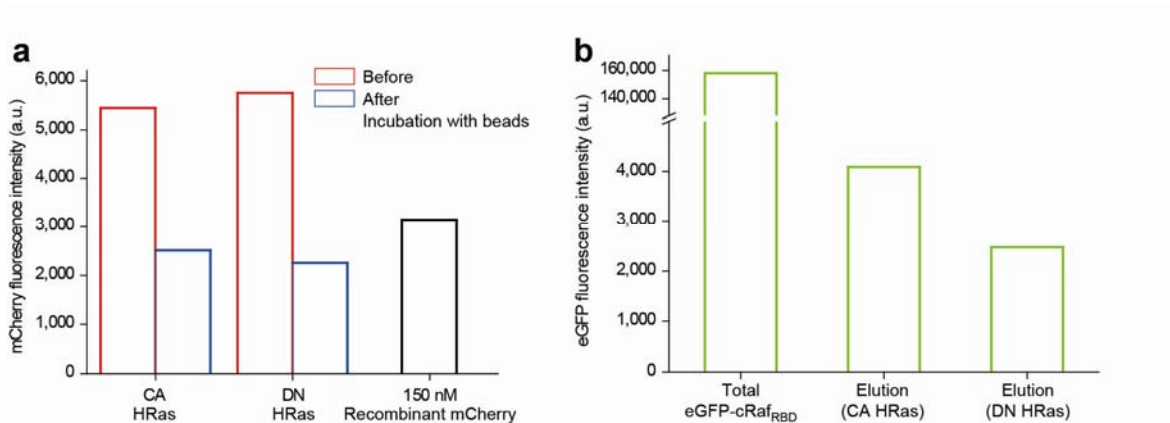
Supplementary References

Supplementary Figures

Supplementary Figure S1. Comparison of conventional co-IP (left), SimPull (middle) and our real-time single-molecule co-IP techniques (right).

**Supplementary Figure S2. Live cell colocalization study of the HRas-cRaf$_{RBD}$ interaction. (a)** The C-terminal CAAX motif of HRas is known to undergo series of post-translational modifications including farnesylation[35]. This post-translational modification is recognized as the indispensable event to translocate HRas to the plasma membrane[36]. We deleted the CAAX motif, which resulted in diffusive distribution of HRas in the cytoplasm. To induce on-demand translocation of HRas to the plasma membrane, we used FKBP-FRB heterodimerization that can be triggered by rapamycin[13]. The FRB domain was fused to Lyn tyrosine kinase. Since the N-terminal 11 amino acids of Lyn contain sites for

myristoylation and palmitoylation, Lyn-FRB is stably anchored to the plasma membrane. The FKBP domain was fused to the CAAX-deleted HRas. When the rapamycin was added, the FKBP-conjugated HRas was captured by the Lyn protein through FKBP-FRB heterodimerization, which effectively translocated HRas to the plasma membrane. The protein-protein interaction between HRas and Ras binding domain of raf1 (cRaf$_{RBD}$) was assessed by seeing whether cRaf$_{RBD}$ was also translocated to the plasma membrane. (**b**) In order to analyze co-localization of HRas and cRaf$_{RBD}$, we measured fluorescence intensity of a specific region of interest (ROI) inside cells. We designated ROI 1 and ROI 2, in which fluorescence intensity changes in the plasma membrane and cytoplasm were recorded, respectively. When constitutively active HRas (Q61L) was translocated to the plasma membrane, the fluorescence signal of HRas in ROI 1 increased by a factor of seven during 10 min imaging, which was accompanied by a decrease in fluorescence signal in ROI 2 to one sixth of the initial value. It is noted that the fluorescence signal of cRaf$_{RBD}$ showed concurrent increase in ROI 1 by a factor of six. When dominant negative HRas (S17N) was used for the same experiment, on the other hand, we observed similar level of HRas translocation to the plasma membrane. However, the cRaf$_{RBD}$ fluorescence levels in both ROI 1 and 2 largely remained unchanged, indicating a minimal interaction between cRaf$_{RBD}$ and dominant negative HRas.

**Supplementary Figure S3. Conventional co-IP analyses of the HRas-cRaf$_{RBD}$ interaction.** The conventional co-IP data in the right panel of Fig. 1b were reassessed by measuring the fluorescence signal of fluorescent protein tags. (**a**) For the co-IP analysis, the mCherry-HRas proteins, either in the constitutively active (CA) or dominant negative (DN) form, were immobilized on beads using the anti-mCherry antibodies. Fluorescence signals measured before and after incubation with beads and comparison with 150 nM recombinant mCherry proteins indicated that ~150 nM HRas proteins were immobilized on beads. A sample volume of 200 µl was used throughout the co-IP experiments. (**b**) The eGFP-cRaf$_{RBD}$ proteins were applied as the prey proteins. The fluorescence level of the original prey protein solution (200 nM eGFP-cRaf$_{RBD}$) was about 1.6×10^5. After the 2 hour reaction at the prey protein concentration of 200 nM, the eGFP-cRaf$_{RBD}$ proteins that had been captured by the HRas proteins on beads were harvested by elution after thorough washing steps. The fluorescence signal of this eluted portion was higher for the reaction with CA HRas than that with DN HRas. However, even this elution portion produced by the CA HRas showed the fluorescence level of 4×10^3, which corresponds to only 2.5% of the original prey proteins. Considering that a tight protein-protein binding would consume 75% of the prey proteins (150 nM baits/200 nM preys), this tiny portion of 2.5% captured during the co-IP process indicates a weak, transient interaction between HRas and cRaf$_{RBD}$ proteins.
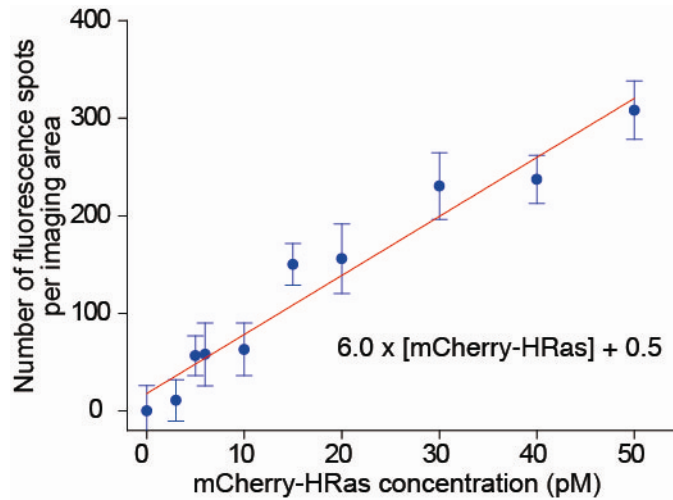
Supplementary Figure S4. Controlling the mCherry-HRas immobilization number on surface. To assess the total immobilization number of bait proteins, we determined the slope for surface immobilization for different bait protein concentrations. The slope was determined by counting the numbers of immobilized single mCherry-HRas proteins while varying the mCherry-HRas concentration. For example, when an anti-mCherry antibody was used for capturing mCherry-HRas as in Figures 1 and 2, the slope was determined to be ~6 count per imaging area/[mCherry-HRas] when [mCherry-HRas] was given in pM. Since one imaging area had an area of 4,050 μm^2 in our TIRF microscopy, we used 350 pM [mCherry-HRas] to locate on average 0.5 mCherry-HRas in each ROI (one ROI has an area of 1.1 μm^2). Since it is presumed that there are more than 10^5 antibodies in one imaging area, the first order approximation should hold well when we immobilize less than 10,000 baits on surface. Error bars denote S.D. (*n*=10).
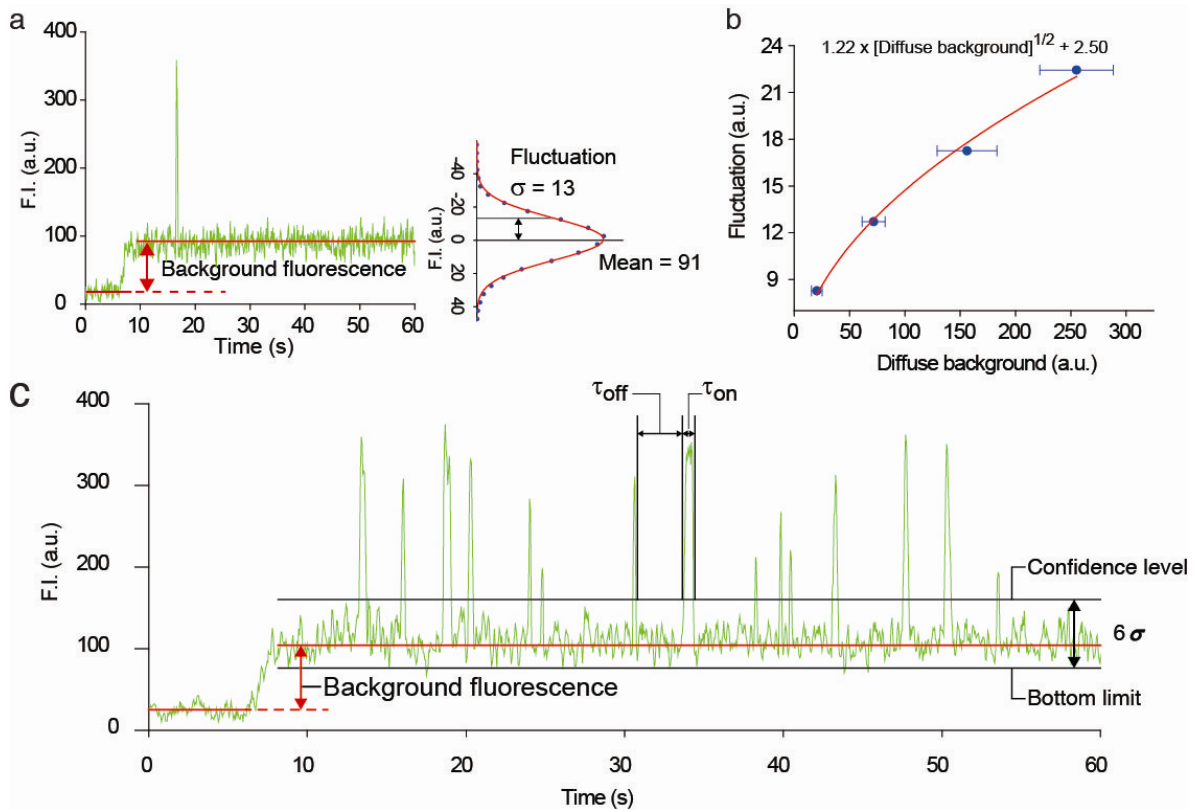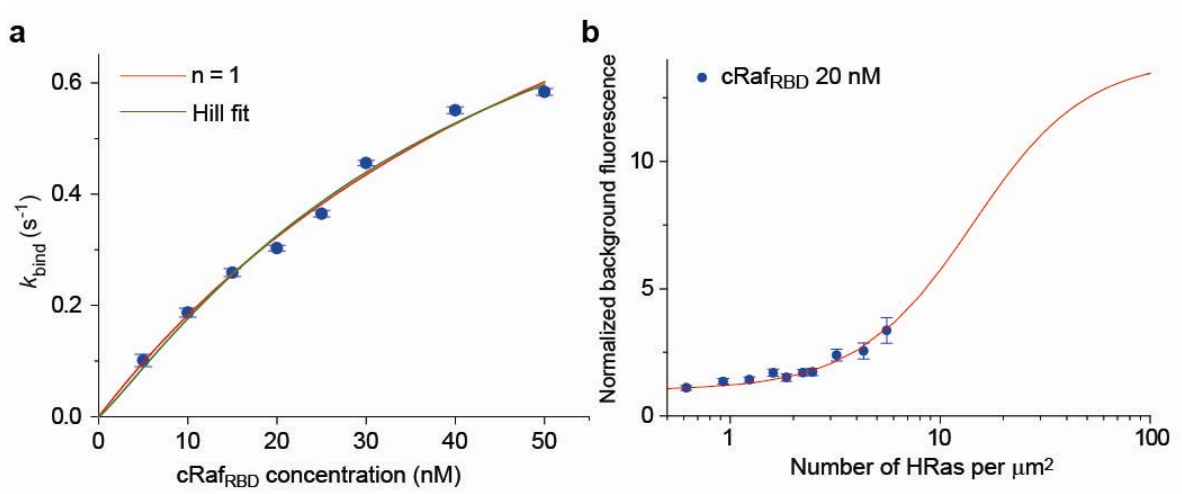
Supplementary Figure S5. Analysis of real-time single-molecule co-IP traces. (**a**) To separate the diffuse background and fluorescence spikes in an objective way, we first obtained the fluctuation information using the reaction with dominant negative HRas. Since this negative control case showed few binding events during 1 min imaging, we were able to clearly separate fluctuations from the fluorescence spikes. The fluctuation was fitted to a Gaussian distribution, which yielded the standard deviation of fluctuation, σ. Moving average with a three point window was applied to real-time traces throughout analysis. (**b**) By increasing the prey protein concentration (eGFP-cRaf$_{RBD}$), we increased the background fluorescence to determine corresponding σ, which gave a calibration curve for σ as a function of the background fluorescence. Error bars denote S.D. ($n>50$). (**c**) To analyze the protein-protein interactions with constitutively active HRas, we first found the background fluorescence from each real-time trace and determined the relevant σ value using the calibration curve of (b). The 20 lowest fluorescence signals were averaged and used as the bottom limit of the individual trace. Six σ above the bottom limit was chosen as the confidence level, which should contain more than 99.9% of the fluctuation. Fluorescence signals that went past the confidence level were considered to be due to specific protein-protein interactions.
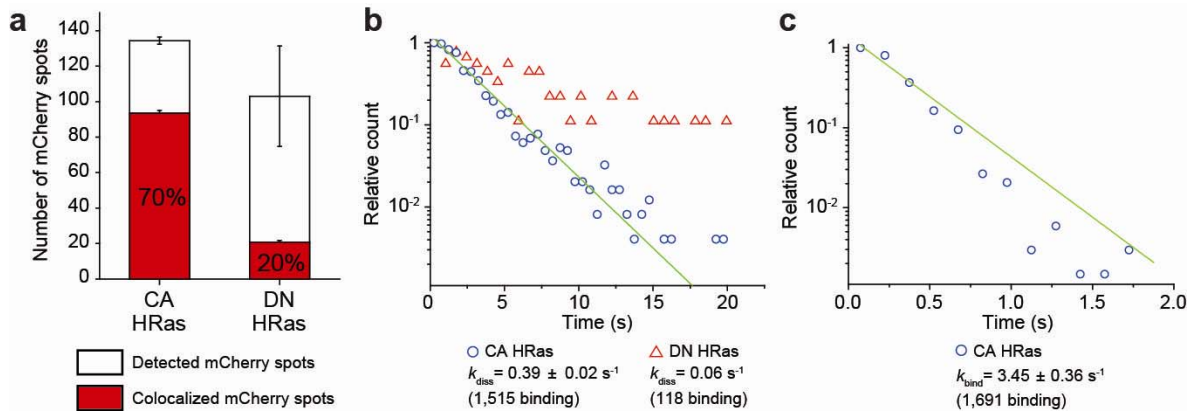
Supplementary Figure S6. Co-localization study for the mCherry-HRas-eGFP-cRaf$_{RBD}$ interaction. (**a**) We used the co-localization method for the HRas-cRaf$_{RBD}$ binding experiment described in Fig. 1. The positions of the pulled-down mCherry-HRas proteins were first identified using a 532 nm laser excitation, and the binding events of 20 nM eGFP-cRaf$_{RBD}$ were selectively recorded from the identified spots. To identify individual mCherry-HRas proteins with minimal overlap, we used a low surface HRas density of ~0.03 HRas per µm^2, in which we had about 130 HRas proteins pulled down per our imaging area. When the mCherry-HRas proteins carried the active mutation (Q61L), approximately 70% of the detected mCherry spots showed any binding events of eGFP-cRafRBD. This percentage, on the other hand, dropped to 20% when the HRas proteins had the dominant negative mutation (S17N), meaning that 80% of the spots showed no binding events. We noted that even with the active mutation, the co-localization percentage was 70% and didn't reach 100%. These 30% spots seemed to be fluorescence junk. (**b**) We analyzed single-molecule kinetics from the identified co-localized spots. When we assessed the binding kinetics from the colocalized spots, the kinetic rates of k_{bind} and k_{diss} were measured to be 0.39 s^{-1} (τ_{off} of 2.51 s) and 3.45 s^{-1} (τ_{on} of 0.29 s), respectively, for the HRas with active mutation. But, the binding frequency, k_{bind}, plunged to 0.063 s^{-1} (τ_{off} of 15.87 s) when the dominant negative HRas proteins were used. All these kinetic rates obtained with the co-localization method are well comparable to those from Fig. 1, in which the surface HRas density is used as the control parameter of the experiments. Errors denotes S.E. (n>80).

Supplementary Figure S7. Kinetic analysis of encounter complex formation. (**a**) The parameter values estimated from fitting the k_{bind} in Fig. 2a using Eq. (6) in Supplementary Text (green line) are n=1.1, $K_1 \approx 43$ nM and κ_{on}=2.16 $s^{-1}nM^{-1}$. If we constrain the Hill coefficient n to be an integer (n=1), the fitting gives $K_1 \approx 67$ nM and κ_{on}=2.78 s^{-1} nM^{-1} (red curve). Error bars denote S.E. (n>200). (**b**) Dependence of normalized diffuse background intensity on the number of HRas per ROI. Fitting the curves to Eq. (14) of Supplementary Text with $n^0_{cRaf_{RBD}}$ 20 nM (red curve) yields values of δ of 0.071. Error bars denote S.D. (n>100).
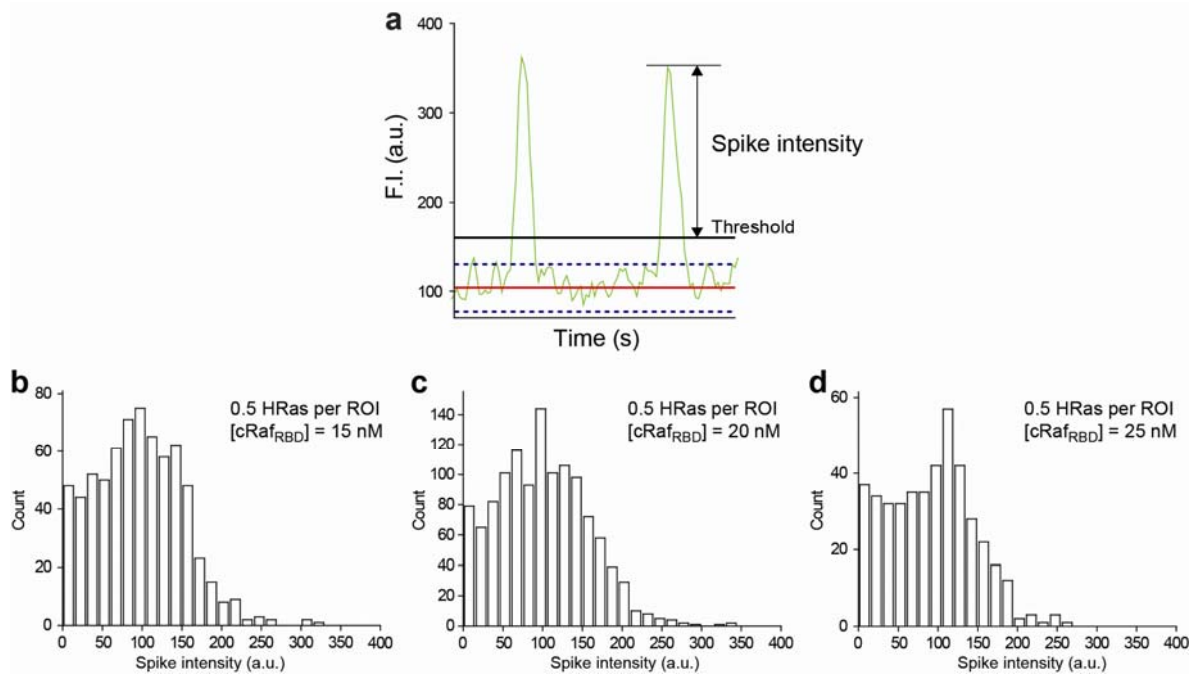
Supplementary Figure S8. Distributions of the fluorescence spike intensity. (a) Fluorescence spike intensity is quantitatively defined as the height of a fluorescence spike above the threshold. **(b-d)** All the histograms of fluorescence spike intensity, obtained at three different prey protein concentrations from 15 to 25 nM, display a unimodal peak at the same position of ~100, which is close to the single eGFP intensity. Nevertheless, we cannot completely rule out the possibility that there are multiple conformations for the final Ras-Raf complex because the histograms show relatively broad distributions around the main peak. However, in every histogram, there is no other appreciable peak that could be attributed to a distinct state. Moreover, both the dwell time kinetics for τ_{on} and τ_{off} can be fitted using single exponential functions (Fig. 1 and 2). Thus, we have presumed one well-defined conformation state for the final Ras-Raf complex throughout our analysis.
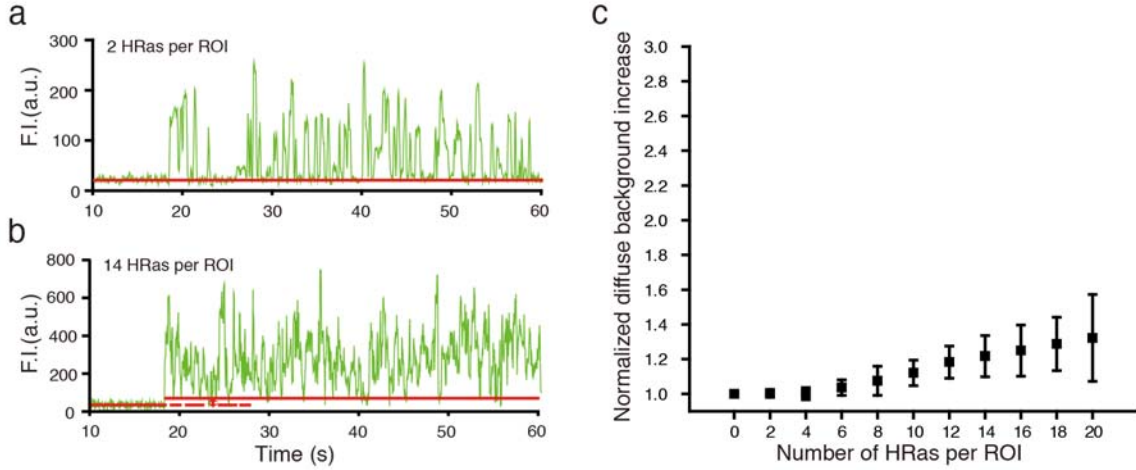
Supplementary Figure S9. Numerical simulation on background fluorescence increase. To investigate if multiple parallel binding events in a single ROI can produce a background fluorescence increase, we have constructed artificial real-time movies of co-IP imaging. In such a movie, a certain number of HRas molecules were distributed randomly on a virtual imaging area consisting of 256×512 pixels. On each HRas molecule, binding and unbinding events of single eGFP-cRaf$_{RBD}$ proteins were stochastically generated following single exponential probability distributions, time constants of which were τ_{off}^{-1} of 1.77 s^{-1} and τ_{on}^{-1} of 3.18 s^{-1}, respectively. A series of images were constructed by placing a two dimensional Gaussian point-spread-function (PSF) on each HRas that was then bound by an eGFP-cRaf$_{RBD}$ molecule. The intensity of a pixel was calculated by the equation,

$$I_{i,j} = \sum_k A \exp[-\frac{(i-x_k)^2 + (j-y_k)^2}{2\sigma^2}],$$ where (i,j) is the position of the pixel under

consideration, (x_k, y_k) is the position of the kth PSF and σ is the standard deviation of the PSF. A is the peak intensity of the PSF that has been adjusted to match the experimental data from Figs. 1 and 2 (A=158.7 used). To simulate shot noise of imaging, a Poisson noise was added for each pixel. It should be noted that in this computer-generated movie, the fluorescence signals only come from the eGFP-cRaf$_{RBD}$ proteins in the final HRas-cRaf$_{RBD}$ complex, without any contribution from freely diffusing cRaf$_{RBD}$s or encounter complexes. The movies were generated as the total HRas numbers were increased up to 76,000, which corresponded to on average 20 HRas per μm^2. In analyzing the movies, we used the same method described in Supplementary Figure S5 to determine the background fluorescence increase from each simulated real-time trace. The background increase found was finally

normalized by the diffuse background (131.1 used here). (**a** and **b**) Exemplary real-time traces simulated with 2 (a) and 14 (b) HRas proteins per μm^2. (**c**) Normalized background fluorescence increase as a function of the number of HRas per μm^2. There is indeed a background fluorescence increase purely by the presence of many parallel binding events in one ROI. However, only 30% increase is obtained even with 20 HRas proteins per μm^2 whereas 300% increase has been observed with 6.2 HRas per μm^2 in our experimental data in Fig. 2f. Thus, it is likely that the presence of multiple parallel binding events cannot be the main cause of the enhancement in background fluorescence, which has been experimentally observed during real-time co-IP. Error bars denotes S.D. ($n>100$).
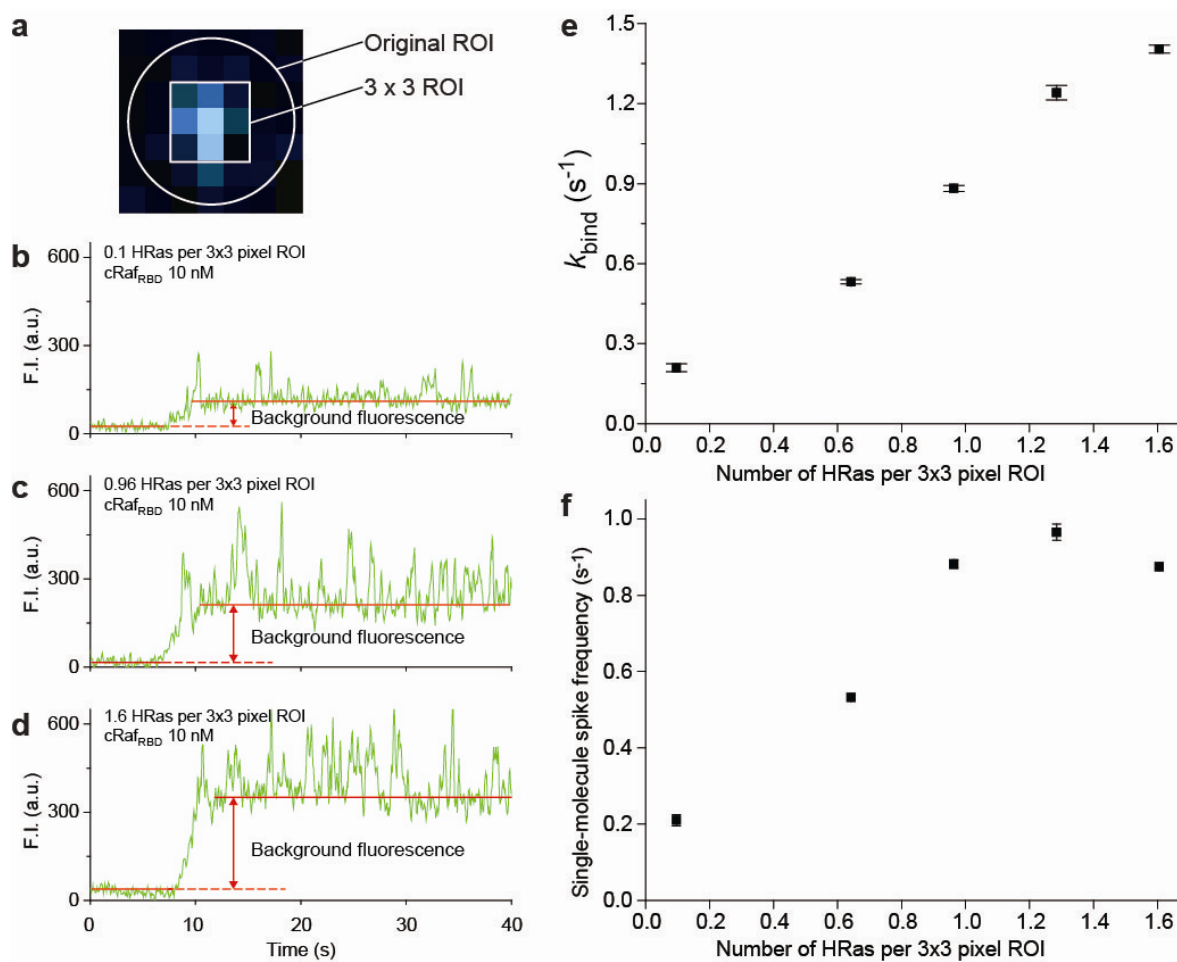
Supplementary Figure S10. Measurement of single-molecule spike frequency in HRas-dense environments. (a) The 3-by-3 pixel ROI used for measuring the single-molecule spike frequency in HRas-dense conditions. This smaller 3×3 pixel ROI has an area of 0.18 μm^2. Our usual ROI is shown as comparison. **(b-d)** Real-time co-IP traces from the same reaction conditions as those for Fig. 2c-e. To obtain these real-time traces, we used the smaller 3×3 pixel ROI and did not apply the Gaussian filter when reading fluorescence signals. The HRas surface density is given as the average number of HRas per 3×3 pixel ROI. **(e)** Resultant k_{bind} measured using the 3×3 pixel ROI for different HRas surface densities. The same procedure described in Supplementary Figure S4 was used. The HRas surface density is given as the number of HRas per 3×3 pixel ROI. (f) The single-molecule spike frequency is given by dividing the k_{bind} of **e** by the average number of HRas each 3×3 pixel ROI contains. When the expected HRas number is smaller than one, k_{bind} is divided by integer one.
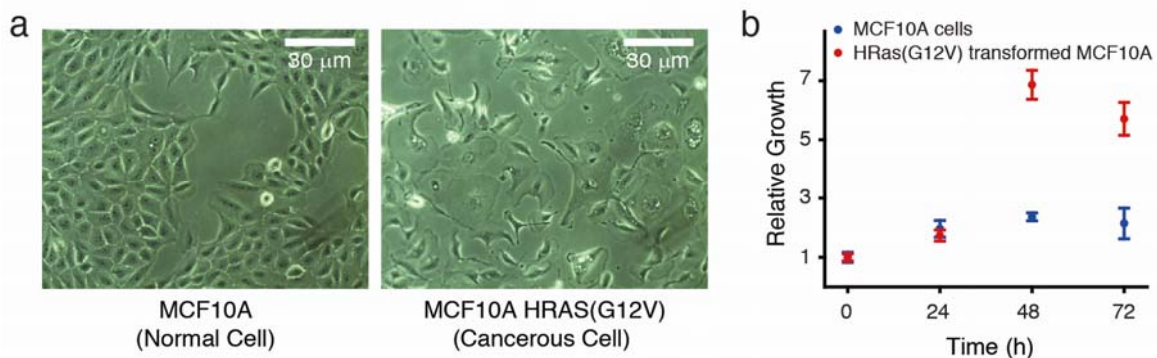
Supplementary Figure S11. Validation of the transformation of immortalized, non-tumorigenic MCF10A cells. (**a**) Morphological changes of MCF10A cells by retroviral HRas (G12V) transduction (right). Parental MCF10A cells are shown as a control (left). After 72 hours since viral transduction, MCF10A cells become irregular in size and shape compared to parental cells, which is considered as a hallmark of cancerous cells. (**b**) The parental MCF10A and transformed MCF10A HRas (G12V) cells were grown in medium devoid of EGF and horse serum. The relative cell number was tracked in time by WST-1 assay. Briefly, WST-1 agent was treated for 1 hour in 37 °C and absorbance at 450 nm was measured. The relative growth was obtained by calculating the fold change in absorbance compared to that measured at 0 hour. The growth rate of transformed MCF10A HRas (G12V) cells was more than twice that of the untransformed MCF10A cells. Error bars denotes S.D. (*n*=3).
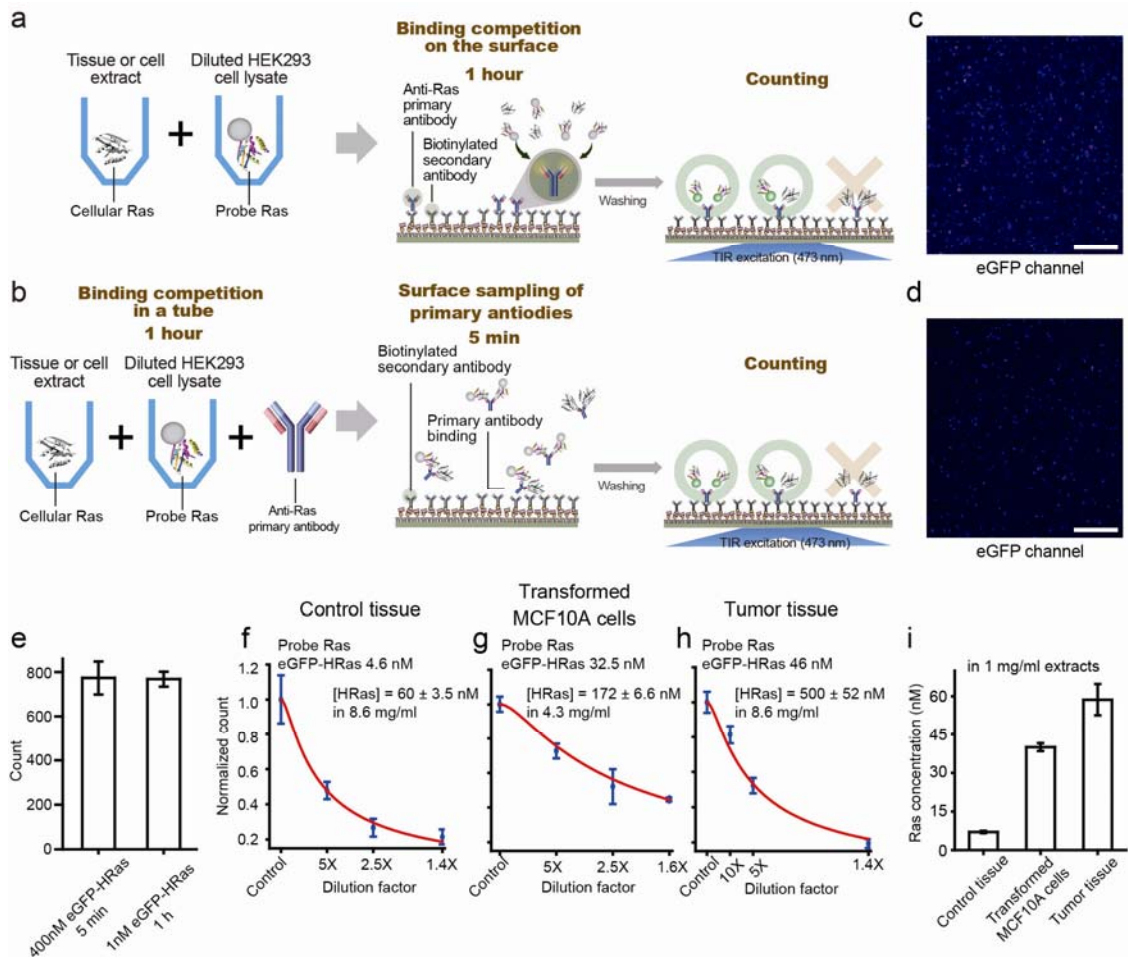
Supplementary Figure S12. Single molecule western analysis. (**a** and **b**) Two experiment schemes for single molecule western analysis. Our single molecule western analysis is based on the competition between cellular and probe proteins for primary antibody binding, which finally saturates the binding sites of the primary antibody. As a result, the analysis does not sensitively depend on the incubation time for surface attachment. The molar concentration of the target cellular protein is determined by the difference in the binding number of target and probe proteins. This binding competition can be induced on surface (a) or in a tube (b). In the case of surface competition, the tandem antibody layer that directly captures both labeled and native proteins was used as the binding surface (a). In the case of competition in a tube, the surface attachment has the effect of sampling the primary antibodies (bound to cellular and probe proteins) on surface (b). Glutaraldehyde could be added to both schemes as a cross-linker to expedite the binding reaction. (**c** and **d**) Although the scheme (a) has been successfully used for measuring the HRas concentration

in transformed MCF10A cells, the scheme (b) has been mainly used for other purposes because it enables to reduce the incubation time of cell or tissue extracts with surface. This shorter incubation time is advantageous when handling tissue extracts because it largely reduces autofluorescence levels coming from nonspecific adsorption of unknown tissue components (c versus d).Scale bar, 10 μm. (**e**) Number of primary antibody per imaging area. By controlling the incubation time, we have tailored the primary antibody number to be suitable for single molecule counting, which is between 500 and 1,000. Incubation of a saturating concentration of probe HRas (eGFP-HRas at 400 nM) for 5 min and 1 nM probe HRas for 1 hour in the presence of the cross-linker gave the same value of 770 as the number of primary antibody per imaging area. (**f-h**) Single-molecule western data for the control tissue (f), transformed cancerous MCF10A cells (g) and cancer tissue (h). (**i**) Concentration of cellular HRas in 1 mg/ml extracts. Error bars denote S.D. (n>20). Numbers following ± sign are S.E.
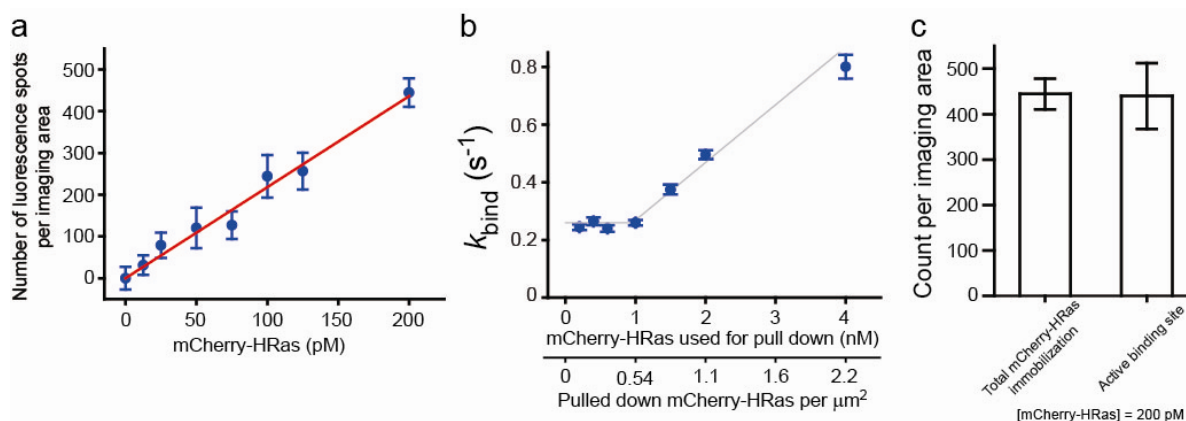
Supplementary Figure S13. Finding the critical density of surface bait proteins for k_{bind} inflation. (**a**) Surface immobilization slope for the tandem antibody layer directly capturing HRas. We employed the same anti-HRas primary antibody that was used for the real-time single-molecule co-IP analyses in Fig. 3f-l. The slope was determined to be 2.2 count per imaging area/[HRas] when [HRas] was given in pM. Thus, at the threshold for k_{bind} inflation observed in Fig. 3l ([HRas]=5.5 nM), we estimate that there are 12,100 HRas proteins immobilized per imaging area. Since our imaging area has an area of 4,050 μm^2, this corresponds to ~3 HRas pulled down per μm^2. (**b**) k_{bind} as a function of the concentration of mCherry-HRas (Q61L) used for pull-down. The threshold for k_{bind} inflation was detected at 1.1 nM [mCherry-HRas], at which 2,400 HRas proteins were estimated to be on the surface. (**c**) Number of active binding spots per imaging area when 200 pM [mCherry-HRas] was pulled down. The number of spots showing active binding events was 440 per imaging area, which was very close to the total Ras immobilization number (443) estimated from (a). Thus, the active fraction of mCherry-HRas (Q61L) closely approximates 100%. This implies that the threshold for k_{bind} inflation occurs when there are 2,400 active baits per imaging area, which corresponds to 0.6 active baits per μm^2. It is noted that this threshold depends only on the geometric parameters of imaging apparatus, not on detailed molecular nature of surface baits. Different size of field of views and/or different algorithm for identifying binding events will shift the number of surface baits required for k_{bind} inflation. But, once it is calibrated for a specific microscope, the threshold will be independent of the molecular nature of surface bait proteins. Error bars denote S.D. for total Ras immobilization (*n*=10) and S.E. for active binding site (*n*=2), respectively.
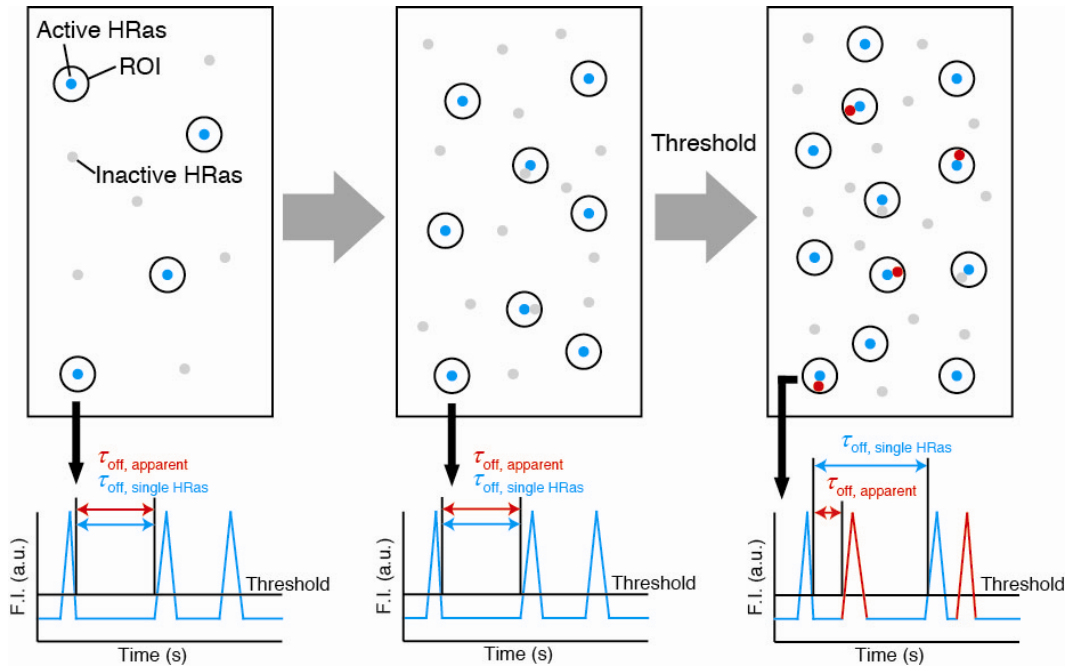
Supplementary Figure S14. Schematics of k_{bind} inflation. Under a diluted condition where the average distance between active HRas is much larger than the diameter of ROI (upper left), the fluorescence spikes from each ROI faithfully reflect the binding events on a single HRas (lower left). The measured $\tau_{off,apparent}$ should be identical to the genuine time constant of single HRas activity, $\tau_{off,single\ HRas}$. Since our imaging area is about 4,000 μm^2 while each ROI has an area of 1.1 μm^2, the imaging area accommodates at least 1,000 active HRas molecules without significant overlapping of their ROIs (upper middle). The $\tau_{off,apparent}$ is constant at the same value, continuously reflecting $\tau_{off,single\ HRas}$ (lower middle). This means that even when the total immobilization number of HRas is increased, the kinetic constant largely stays at the same value up to a certain point. However, if the total immobilization number is increased beyond a certain threshold, more than one active HRas molecules begin to be included in some of ROIs (upper right). These additional HRas molecules create additional fluorescence spikes (lower right, red spikes), which make $\tau_{off,apparent}$ smaller than the genuine $\tau_{off,single\ HRas}$. As a result, the measured kinetic rate of $k_{bind,apparent}$ is expected show a biphasic behavior as a function of total HRas immobilization number. The $k_{bind,apparent}$ is initially maintained at a constant of $k_{bind,single\ HRas}$, but begins to increase beyond the threshold. We note that this threshold for $k_{bind,apparent}$ corresponds to a specific surface density of active baits, which is independent of detailed molecular nature of bait proteins. Thus, comparing the thresholds can be directly used to assess the active portion of bait proteins on surface.
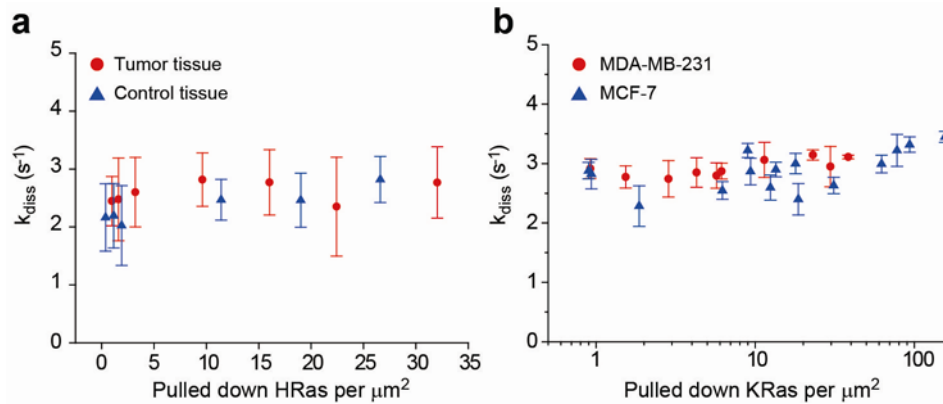
Supplementary Figure S15. k_{diss} observed for native signaling Ras. Unlike k_{bind} that shows inflation past the thresholds (Fig. 3l and Fig. 4c), k_{diss} is largely constant for every HRas and KRas sample we studied. We note that τ_{on} values are in the range of hundreds of ms, showing that the rapid turnover in Figs. 1 and 2 is also observed for the native Ras pulled down from both tumor and control tissues.
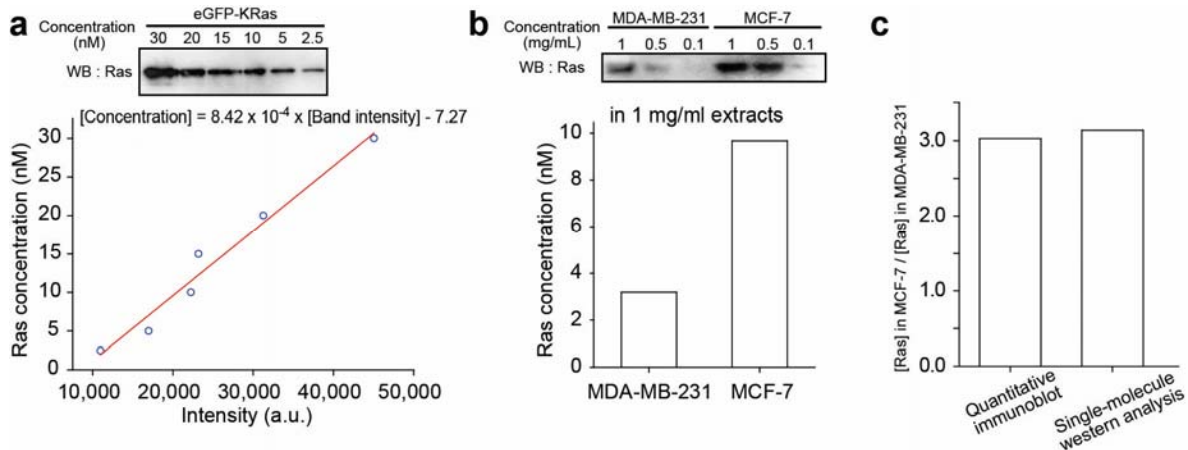
Supplementary Figure S16. Quantitative KRas immunoblot of MDA-MB-231 and MCF-7 cells. (a) External calibration for quantitative KRas immunoblotting. eGFP-KRas plasmid transfected HEK293 cell lysates were serially diluted from 0.1 nM to 30 nM and run on the SDS-PAGE gel followed by immunoblot (20 µL was loaded in each lane). Signal intensities of each diluent were quantified using ImageJ. Because 1 nM and lower concentration of eGFP-KRas were not detected, we plotted concentration [nM] versus band intensity from 2.5 nM to 30 nM and it showed linear relationship of concentration against intensity. (**b**) We performed quantitative immunoblotting to double-check the KRas concentrations in the MCF-7 and MDA-MB-231 cells in Fig. 4. Because signal intensity was too weak at 0.5 mg/mL and lower, we selected the cases of 1 mg/mL lysate to calculate the Ras concentrations from the standard curve of a. The KRas concentrations are 3.2 nM for MDA-MB-231 and 9.7 nM for MCF-7 in 1 mg/mL cell extracts, respectively. These values are little bit lower than those from our single-molecule western analysis from Fig. 4 (5.5 and 17.3 nM), which seems to be due to loss of proteins during transfer to PVDF membrane prior to immunoblotting. (**c**) We however note that the Ras-concentration ratio of MCF-7 to MDA-MB-231 is 3.03 (9.7 nM/3.2 nM), which is very close to the value of 3.14 (17.3 nM/5.5 nM) estimated by the single-molecule western analysis. This reconfirms our important finding that the mutant KRas in MDA-MB-231 cells has a smaller concentration than the wild-type KRas in MCF-7 cells.

Supplementary Table

[cRaf$_{RBD}$] (nM)	Apparent dissociation constant $\dfrac{k_{diss}}{k_{bind}}$ [cRaf$_{RBD}$] (nM)
15	160.2
20	196.8

	K_D (nM)
Ref. 12	160
Ref. 37	130

Supplementary Table S1. Comparison of the dissociation constants measured in this work with the previous bulk assay data. The apparent dissociation constants were obtained from real-time co-IP traces by measuring k_{diss} and k_{bind} and calculating $\dfrac{k_{diss}}{k_{bind}}$ [cRaf$_{RBD}$]. The cRaf$_{RBD}$ concentrations of 15 and 20 nM were used because they were the midpoints of the concentration range we studied. The measured apparent dissociation constants are 160.2 and 196.8 nM, which are close to the K_D values of 160 (ref.12) and 130 nM[37] reported from previous bulk assay data. Such similar results are not very surprising because in our real-time imaging of the HRas-cRaf$_{RBD}$ interaction from Figs. 1 and 2, both the bait and prey proteins were studied under an overexpressed condition. The labeled proteins were larger than endogeneous counterparts in number by two orders of magnitude. Thus, the measured HRas-cRaf$_{RBD}$ kinetics becomes not very different from what have been measured using purified, recombinant proteins. Also, this close consistency with the bulk assay data implies that the surface immobilization of HRas proteins does not seriously affect its interaction with cRaf$_{RBD}$.

Supplementary Methods

Kinetic scheme of the HRas-cRaf$_{RBD}$ interaction

In the real-time single-molecule co-IP experiment that probes the HRas-cRaf$_{RBD}$ interaction using TIRF over an ROI, HRas molecules are immobilized on the surface and cRaf$_{RBD}$ proteins tagged with eGFP are either (i) free to diffuse over the space, in (ii) an encounter complex state ([HRas···cRaf$_{RBD}$]) or in (iii) an active state (HRas·cRaf$_{RBD}$) that gives rise to the "on" signal. In the experiment, the inter-HRas distance is large enough so that each cRaf$_{RBD}$ can interact with one immobilized HRas on the surface. To account for our measurement associated with the dynamics between HRas and cRaf$_{RBD}$, we propose a reaction scheme as follows:

$$\text{HRas} + \text{n} \cdot \text{cRaf}_{RBD} \underset{k_{-1}}{\overset{k_1}{\rightleftharpoons}} [\text{HRas} \cdots (\text{cRaf}_{RBD})_n] \underset{\kappa_{off}}{\overset{\kappa_{on}}{\rightleftharpoons}} \text{HRas} \cdot (\text{cRaf}_{RBD})_n \quad (1)$$

where k_1 and k_{-1}, respectively, are the diffusion-limited association and dissociation rate constants to form the encounter complex; κ_{on} and κ_{off} are the forward and backward rate constants for the transition kinetics between the encounter and active complexes. Note that the above kinetic scheme considers a stoichiometry of 1:n between HRas and cRaf$_{RBD}$. In this reaction scheme, the probability of forming the encounter complex [HRas···(cRaf$_{RBD}$)$_n$] is deemed to account for the level of background fluorescence.

Since the background intensity remains constant throughout the measurement, we surmise that the encounter complex [HRas···(cRaf$_{RBD}$)$_n$] reaches a fast pre-equilibrated steady state, i.e., time scale of encounter complex formation from free cRaf$_{RBD}$ is much faster than the transition between "on" and "off" states ($k_1, k_{-1} >> \kappa_{on}, \kappa_{off}$). At pre-equilibrium state, the condition of detailed balance gives rise to

$$k_1 \, n_{\text{HRas}}^{ss} \left(n_{\text{cRaf}_{RBD}}^{ss} \right)^n = k_{-1} \, n_{\text{HRas} \cdots (\text{cRaf}_{RBD})_n}^{ss} \quad (2)$$

where n_X^{ss} is the number of X molecules per unit ROI volume. Using the conditions of mass balance $n_{\text{HRas}}^{ss} + n_{\text{HRas} \cdots (\text{cRaf}_{RBD})_n}^{ss} = n_{\text{HRas}}^0$ and $n_{\text{cRaf}_{RBD}}^{ss} + n \cdot n_{\text{HRas} \cdots (\text{cRaf}_{RBD})_n}^{ss} = n_{\text{cRaf}_{RBD}}^0$, one can formally solve $n_{\text{HRas} \cdots (\text{cRaf}_{RBD})_n}^{ss}$ as a function of $n_{\text{HRas}}^0, n_{\text{cRaf}_{RBD}}^0$ and microscopic rate constants.

The transition rate to the "on" signal (k_{bind} from TIRF signal) corresponds to κ_{on} multiplied by the probability of cRaf$_{RBD}$ being in the encounter complex:

$$\frac{1}{\tau_{off}} = \kappa_{on} n^{ss}_{HRas\cdots(cRaf_{RBD})_n} \quad (3)$$

τ_{on} is the time constant of inactivation, which is independent of other HRas-cRaf$_{RBD}$ complexes:

$$\frac{1}{\tau_{on}} = \kappa_{off} = k_{diss} \quad (4)$$

While it is difficult to obtain an algebraically tractable solution for Eq.(2), we note the experimental condition $n^{ss}_{HRas\cdots(cRaf_{RBD})_n} << n^0_{cRaf_{RBD}}$ is well satisfied in the τ_{off} measurement of Fig. 1. We can then approximate the occupancy of this one HRas protein, $n^{ss}_{HRas\cdots(cRaf_{RBD})_n}$,

using a Hill-type equation by defining $(K_1)^n \equiv \dfrac{k_{-1}}{k_1}$ for general n:

$$n^{ss}_{HRas\cdots(cRaf_{RBD})_n} \approx \frac{n^0_{HRas}(n^0_{cRaf_{RBD}}/K_1)^n}{1+(n^0_{cRaf_{RBD}}/K_1)^n} \quad (5)$$

Therefore, from Eq.(3),

$$k_{bind} = \kappa_{on} n^{ss}_{HRas\cdots(cRaf_{RBD})_n} \approx \kappa_{on} \frac{n^0_{HRas}(n^0_{cRaf_{RBD}}/K_1)^n}{1+(n^0_{cRaf_{RBD}}/K_1)^n} \quad (6)$$

Measurement of k_{bind} indeed shows hyperbolic dependence on $n^0_{cRaf_{RBD}}$, indicating the Hill coefficient $n=1$. The effective HRas concentration, n^0_{HRas}, was obtained by finding the average inter-HRas distance and the corresponding three-dimensional concentration, which gave $n^0_{HRas} = 1.44 \cdot (\text{Number of HRas per ROI})^{3/2}$ nM. The parameter values estimated from a numerical fit using Eq. (6) (solid line) are $n=1.1 \rightarrow 1$, $K_1 \approx 67$ nM and $\kappa_{on} = 2.78$ s^{-1}nM^{-1},

justifying 1:1 stoichiometry for the HRas-cRaf$_{RBD}$ interaction (Supplementary Fig. S6). Alternatively, one can check how apparent $k_{on} = k_{bind} (n^0_{cRaf_{RBD}})^{-1}$ depends on $n^0_{cRaf_{RBD}}$. If

$n \geq 2$, k_{on} would be an increasing function of $n^0_{cRaf_{RBD}}$.

Fluorescence intensity of the diffuse background

TIRF microscopy detects eGFP-cRaf$_{RBD}$ molecules with the signal intensity proportional to

$$I(t) = I_{on}(t) + I^{ss}_{bg}, \qquad (7)$$

where $I_{on}(t) \propto n_{HRas \cdot cRaf_{RBD}}(t)$ is the "on" signal above the diffuse background contributed by

the eGFP-cRaf$_{RBD}$ in the HRas·cRaf$_{RBD}$ complex. I^{ss}_{bg} is due to the amount of (i) encounter

complex [HRas···cRaf$_{RBD}$] and (ii) freely diffusing cRaf$_{RBD}$ within the TIRF zone:

$$I^{ss}_{bg} \propto n \cdot n^{ss}_{HRas \cdots (cRaf_{RBD})_n} + n^{ss}_{cRaf_{RBD}} \delta \approx n \cdot n^{ss}_{HRas \cdots (cRaf_{RBD})_n} + n^0_{cRaf_{RBD}} \delta, \qquad (8)$$

where δ is a numerical factor that takes into account the contribution of free cRaf$_{RBD}$ to the

TIRF intensity, relative to that of encounter complex. In the last line, $n^{ss}_{cRaf_{RBD}} \approx n^0_{cRaf_{RBD}} \delta$

was used because only a handful of cRaf$_{RBD}$ molecules participates in interacting with HRas in one ROI, i.e., the bulk concentration of cRaf$_{RBD}$ is little affected by the presence of HRas-cRaf$_{RBD}$ interaction. Eq. (8) proposes that the background signal increase with both HRas and cRaf$_{RBD}$ molecule in an ROI. Normalized with the dominant negative HRas case

($n^{ss}_{HRas \cdots (cRaf_{RBD})_n} \to 0$ or $K_1 \to \infty$), Eq. (8) should read

$$I^{norm}_{bg} = \frac{I^{ss}_{bg}}{n^0_{cRaf_{RBD}} \delta} = 1 + \delta^{-1} \frac{n \cdot n^{ss}_{HRas \cdots (cRaf_{RBD})_n}}{n^0_{cRaf_{RBD}}} \qquad (9)$$

Since $n = 1$, it is straightforward to perform the analysis by using algebraically tractable solution of Eq.(2):

$$n^{ss}_{HRas \cdots cRaf_{RBD}} = \frac{1}{2} \left[(n^0_{HRas} + n^0_{cRaf_{RBD}} + K_1) - \sqrt{(n^0_{HRas} + n^0_{cRaf_{RBD}} + K_1)^2 - 4 n^0_{HRas} n^0_{cRaf_{RBD}}} \right] \qquad (10)$$

A limiting condition $n_{\mathrm{HRas\cdots cRaf_{RBD}}}^{ss} \ll (n_{\mathrm{HRas}}^{0} + n_{\mathrm{cRaf_{RBD}}}^{0} + K_1)$, which indeed corresponds to our experimental condition, further simplifies Eq. (10) to:

$$n_{\mathrm{HRas\cdots cRaf_{RBD}}}^{ss} \approx \frac{n_{\mathrm{HRas}}^{0} n_{\mathrm{cRaf_{RBD}}}^{0} / K_1}{1 + (n_{\mathrm{HRas}}^{0} + n_{\mathrm{cRaf_{RBD}}}^{0}) / K_1} \qquad (11)$$

which is reduced to Eq.(5) when applied to a single HRas with $n=1$ and $n_{\mathrm{HRas}}^{0} \ll n_{\mathrm{cRaf_{RBD}}}^{0}$.

Finally, we obtain analytical expression for k_{bind} and I_{bg}^{ss} as follows

$$k_{\mathrm{bind}} \approx \kappa_{on} \frac{n_{\mathrm{HRas}}^{0} n_{\mathrm{cRaf_{RBD}}}^{0} / K_1}{1 + (n_{\mathrm{HRas}}^{0} + n_{\mathrm{cRaf_{RBD}}}^{0}) / K_1}, \qquad (13)$$

$$I_{bg}^{norm} \approx 1 + \delta^{-1} \frac{n_{\mathrm{HRas}}^{0} / K_1}{1 + (n_{\mathrm{HRas}}^{0} + n_{\mathrm{cRaf_{RBD}}}^{0}) / K_1}. \qquad (14)$$

Supplementary References

35   Winter-Vann, A. M. & Casey, P. J. Post-prenylation-processing enzymes as new targets in oncogenesis. *Nat. Rev. Cancer* **5**, 405-412 (2005).

36   Hancock, J. F., Paterson, H. & Marshall, C. J. A polybasic domain or palmitoylation is required in addition to the CAAX motif to localize p21ras to the plasma membrane. *Cell* **63**, 133-139 (1990).

37   Kiel, C. *et al.* Improved binding of raf to Ras.GDP is correlated with biological activity. *Journal of Biological Chemistry* **284**, 31893-31902 (2009).